Viscoelastic properties of electrospray-deposited polymer shells via quartz crystal microbalance with dissipation (QCM-D)

Robert A. Green-Warren[1, §], Noah M. McAllister[1], Parameshwaran Pasupathy[1], Assimina A. Pelegri[1], Jonathan P. Singer[1], N. Sanjeeva Murthy[*,2]*

Department of Mechanical and Aerospace Engineering, Rutgers University, Piscataway, NJ, 08854, USA
Laboratory for Biomaterials Research, Department of Chemistry and Chemical Biology, Rutgers University, Piscataway, NJ, 08854, USA

N.S. Murthy
Laboratory for Biomaterials Research, Department of Chemistry and Chemical Biology, Rutgers University, Piscataway, NJ, 08854, USA
E-mail: nsmurthy@chem.rutgers.edu

Keywords: Polymer shells, nanoparticles, thin films, electrospray deposition, viscoelasticity, quartz crystal microbalance with dissipation

Abstract

Viscoelastic properties of polymer nanoshell coatings fabricated by electrospray deposition (ESD), on gold-coated quartz crystals and spin-coated polystyrene (PS) surfaces, were evaluated using Quartz Crystal Microbalance with Dissipation (QCM-D). For PS particles on gold, as ESD flow rate increases from 0.5 to 1.5 mL/h, film thickness increases from ~200 to 400 nm, while dissipation increases by an order of magnitude. This is attributed to larger particle sizes resulting from shorter droplet flight times during ESD. Absence of this effect on spin-coated PS films suggest complex interfacial interactions between ESD PS shells and spin-coated PS films. Shear moduli for ESD coatings on gold are found to be virtually independent of flowrate (i.e. particle size) and are consistent with literature on expanded polystyrene foams. While the QCM-D modulus of the spray coated film is only 0.08-0.20% of the bulk PS modulus, the stiffness ratio of spray coated PS to a single shell is 5.00 - 13.3 x 10^3 m^{-1}, due the more rigid response arising from shell-shell and shell-substrate interactions. These results underscore QCM-D, with nanograms of material, has the potential to predict the mechanical properties of particulate viscoelastic films suitable for high surface area sensor applications such as size-selective membranes relevant to protein or electrolyte adsorption.

1. Introduction

Porous polymer films are emerging as critical components of numerous engineering applications including gas separations, desalination, aerosol capture, and energy storage systems. Polymer films can be synthesized through various methods of polymer-solvent phase separation and are often categorized as supported or free-standing films. Supported films can be produced by drop casting,

spin coating, and electrospray deposition (ESD), whereas free standing films are commonly generated through a process such as phase inversion.[1-4]

ESD is a technique notable for its ability to generate uniform polymer films with tunable morphologies.[5-8] Tunability, i.e., fine control of the microstructure, thickness, and porosity is achieved through manipulation of the electrospray parameters, such as input voltage, polymer-solvent concentration, separation distance, and solution conductivity.[5, 9] In the self-limiting electrospray deposition (SLED) regime, electrostatic charge build-up leads to the formation of conformal micron-scale porous coatings on 2D and 3D surfaces.[4, 6, 10] The ability of SLED to coat both conductive and non-conductive surfaces is highly advantageous for coating various materials, with past and current examples including, most commonly, metals and semiconductors, but also glass, hydrogels, living tissue, and gold plated quartz.[11-13] Additionally, SLED is capable of producing nanoscale and microscale particles, leading to desirable surface characteristics such as super hydrophobicity and hydrophilicity, resulting in films with tunable absorption and adsorption properties.[14, 15] These coatings are generally in the form of partially fused polymeric shells because of the evaporation kinetics of the solvent and the viscosity of PS; other morphologies, including

nanowires, can also be generated.[4, 10] An illustration of the gold-plated QCM sensor after electrospray (ES) is shown in **Figure 1**.
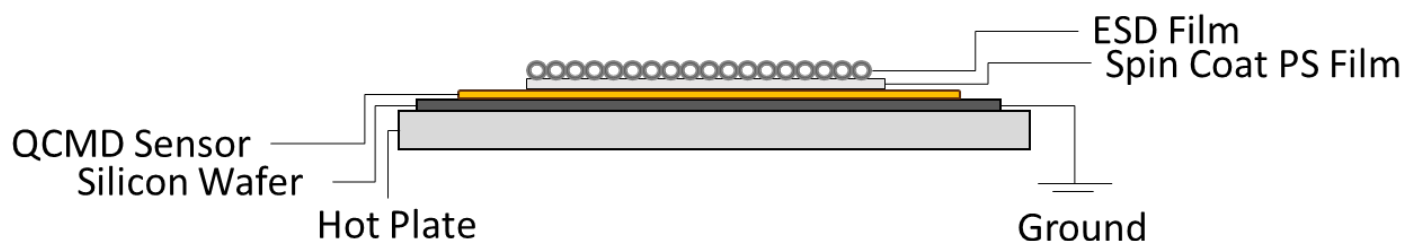

Figure 1. Schematic of the coated layers leading to a monolayer of PS particles atop a spin coated PS layer, and finally the quartz sensor. Silicon wafer is used as a ground and the hotplate can be used to adjust substrate temperature.

The coatings deposited in this work are sprayed in the SLED regime, but since the thickness is too small to trigger the self-limiting effect, it will be simply referred to as ESD films.

In our previously published report of the mechanical characterization of SLED films, we demonstrated the effects of film morphology on the quasistatic mechanical response of SLED films using various model polymers.[5] Nanoindentation with a conospherical tip was used to evaluate SLED film response to compressional loads at low strain-rates. Further, laser induced projectile impact test (LIPIT) is often utilized to evaluate a materials ability to dissipate the energy of high speed impact using ceramic or polymer based microprojectiles, 3-30 µm in diameter.[16] Ren et al. compared LIPIT and sphero-conical nanoindentation results from PS by evaluating volumetric energy dissipation.[17] They show that the primary source of dissipation during nanoindentation is due to the collapse of the hollow particles. In contrast, thermo-mechanical annealing and crazing were significant contributors to energy dissipation under high-speed impact, in the range of 200-

4

900 m/s.[17] However, it was found that at depths greater than 50% of the original film thickness, substrate rigidity and particle confinement effects also contribute to the elastic behavior of SLED films under both loading conditions.[5, 17] Since both nanoindentation and LIPIT suffer from effects of confinement, film-substrate interactions, and loading configuration such as indenter tip size for nanoindentation and projectile size for LIPIT, alternative methods to evaluate the mechanical behavior of ESD films are necessary to fully characterize them across a wide spectrum of strain rates.

In this paper, we introduce quartz crystal microbalance with dissipation (QCM-D) to evaluate the morphology and mechanical properties of ESD films. QCM uses the mass dependence of the resonance frequency (~ 5 MHz) of a piezoelectric quartz crystal to measure nanogram changes in mass by measuring frequency changes (Δf) with a precision of 1-2 Hz. In QCM-D, instead of continuous oscillation of the crystal, the crystal is pinged at millisecond intervals to observe the decay of these oscillations. The rate and magnitude of this decay is use to changes in dissipation (ΔD).[18] Because lower frequency oscillations propagate farther away from the surface than higher frequency ones, it is possible to capture the depth-dependence of the viscous properties of the layers deposited onto the gold surface by monitoring several harmonics. Such measurements and detailed analysis of multiple harmonics can be used to examine the mechanical response of ESD

particles to shear stresses at megahertz frequencies.[19] An example set of electrosprayed Au-plated quartz sensors is shown in **Figure 2**.
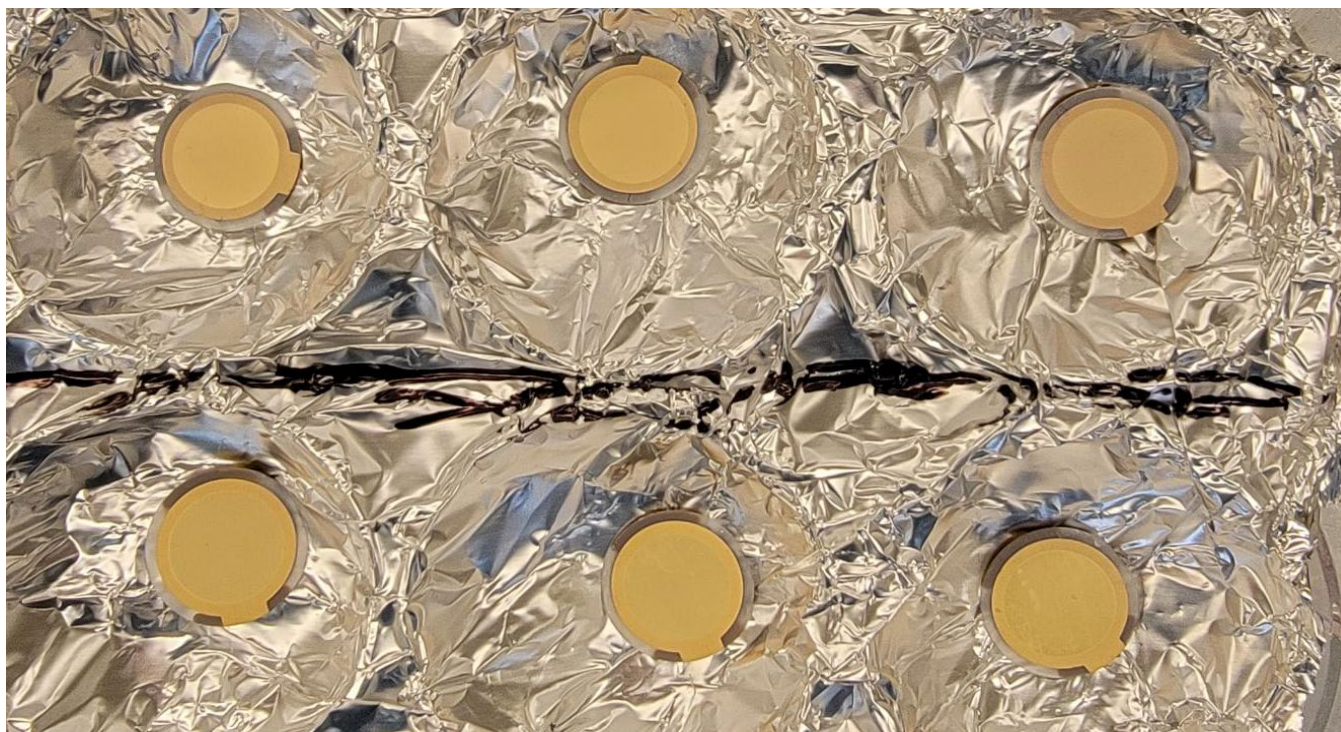

Figure 2. Six gold plated quartz crystal after electrospraying with a thin layer of PS particles.

2. Results and Discussion

ESD films with thicknesses between 10^1-10^2 µm can be measured via optical microscopy. Since the particles of the ESD PS coatings are often too small to be resolved at visible wavelengths, they are typically evaluated using SEM.[20, 21] **Figure 3** is a top-down view of an ESD coating deposited onto a silicon (Si) wafer obtained via SEM. Particle diameters in the range 1-10 µm, decorated with secondary smaller particles <1 µm, have been observed for the electrospray parameters used

in this study.[5] The morphology of polymer shells is largely dictated by solution flow rate, solvent

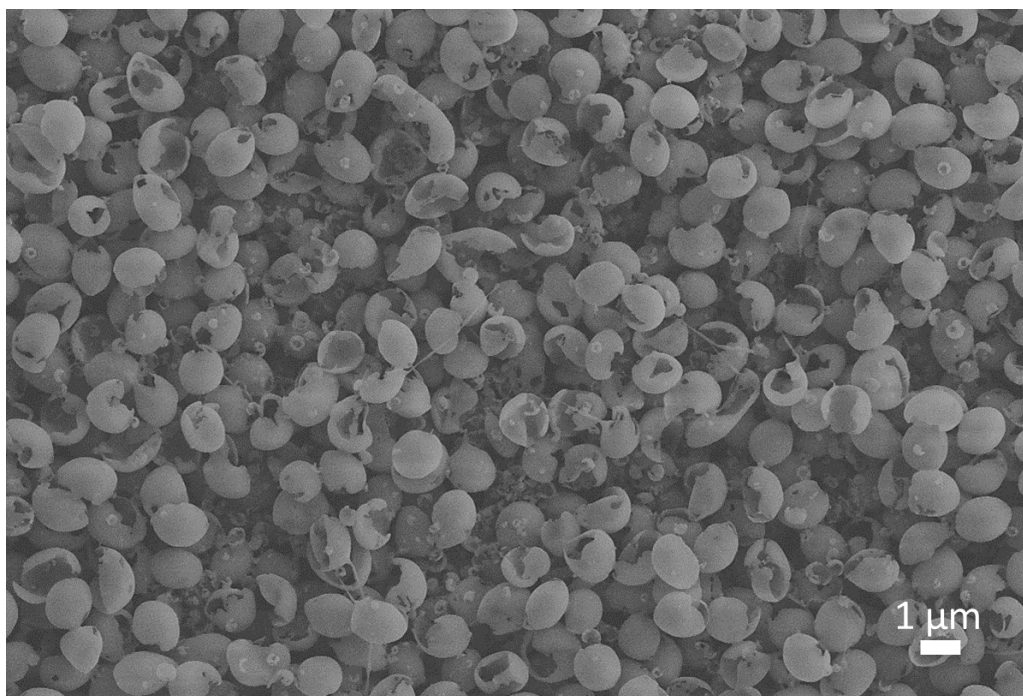evaporation kinetics, and viscosity of the polymer-solvent blend.[4, 22]

Figure 3. Top-down image of a PS ESD film on a silicon wafer sprayed at a flow
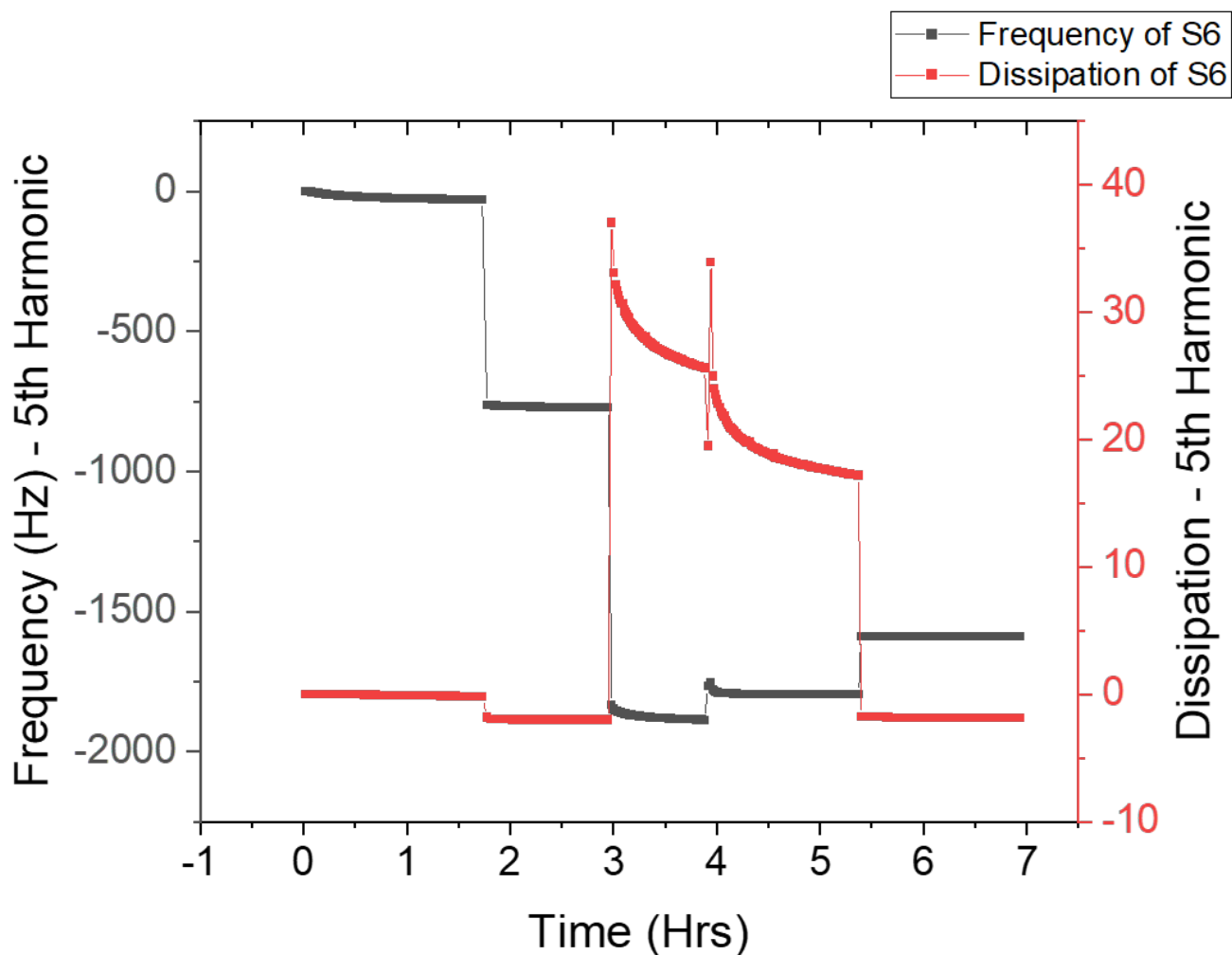
rate of 0.5 mL/hr.

Figure 4. Raw frequency and dissipation data plot for sensor 6 (S6).

QCM-D measurements consisted of measuring the Δf and ΔD data sequentially on bare QCM-D sensors (S1-S8) as a benchmark, after spin coating one layer of PS (S5-S8), after spray coating (S1-S8), after ambient aging for ~24 hours (S1-S8), and finally, after thermal annealing (S1-S8). **Figure 4** is a representative plot of the Δf and ΔD shifts for S6, which was obtained by stitching each curve into one data frame. The plots for all other sensors can be found in **Figures S1 - S4**. The results for sensor S6 are summarized in **Table 1**. The morphology of the porous PS films

8

deposited via ESD onto bare gold surface (S1-S4) and onto spin-coated PS surface (S5-S8) were similar.

2.1 Frequency and dissipation changes

The data in Figure 4 are split into five distinct sections corresponding the coating conditions. While Δf, to a first approximation, represents the change in mass or thickness of an adsorbed layer, ΔD reflects the viscoelastic and plastic behavior of this layer. The decrease in Δf at ~1.8 h arises from the addition of the spin coat PS layer, whose Sauerbrey mass is ~14 μg. Negative dissipation values are observed (Table 1) for the spin coated film. However, since these values are very small (ΔD ~2 x 10^{-6} -10^{-7} for Δf of 10^2 -10^3 Hz), they can be approximated to be zero. These zero shifts in ΔD indicates that the films are rigid and strongly bound to the gold substrate. The similarities in Δf and ΔD values for sensors S5-S6 and S7-S8 (Table 1) is indicative of the uniform mass deposition of the spin coated PS film for these crystals. The second shift at ~3 h reflects the addition of the spray coated PS particles. The decrease in Δf corresponds to the additional spray deposited PS particles. The dramatic increase in ΔD is due to viscoelastic behavior of the hollow spheres. The third change in Δf induced at ~ 4-hour mark was caused by the removal of the sensor and reinserting it after aging at ambient conditions for 24 h, to continue the data collection. The positive shift in frequency does not indicate mass loss, but rather significant change in material's behavior or microstructure during aging.[19] There is evidence of plastic behavior within the polymer network, which appears to be a secondary mode of deformation for this segment of the testing sequence. This could explain a decrease in energy dissipation at 4 h after aging. The fifth and final

9

change in Δf highlights the effect of thermal annealing. Here, Δf increases and ΔD returns to the initial value (~1.8 h mark) as the PS particles fuse into a smooth and rigid thin film free of porosity. The two sets of gold substrates with spray coated films (S1, S2 and S3, S4, deposited at 0.5 and 1.5 ml/h for 18 and 6 minutes, respectively) contained same volume of solution, 0.15 ml. Interestingly, film thickness doubles from ~200 to ~400 nm when the flow rate increases from 0.5 to 1.5 ml/h, respectively. The dissipation increases by approximately a factor of 20 from ~40 in S1-S2 to ~700 x 10^{-6} in sensors S3-S4; the latter of which was sprayed at the higher flow rate. Indicating that ESD films fabricated at lower flow rates behavior more rigidly than those sprayed at higher flow rates.
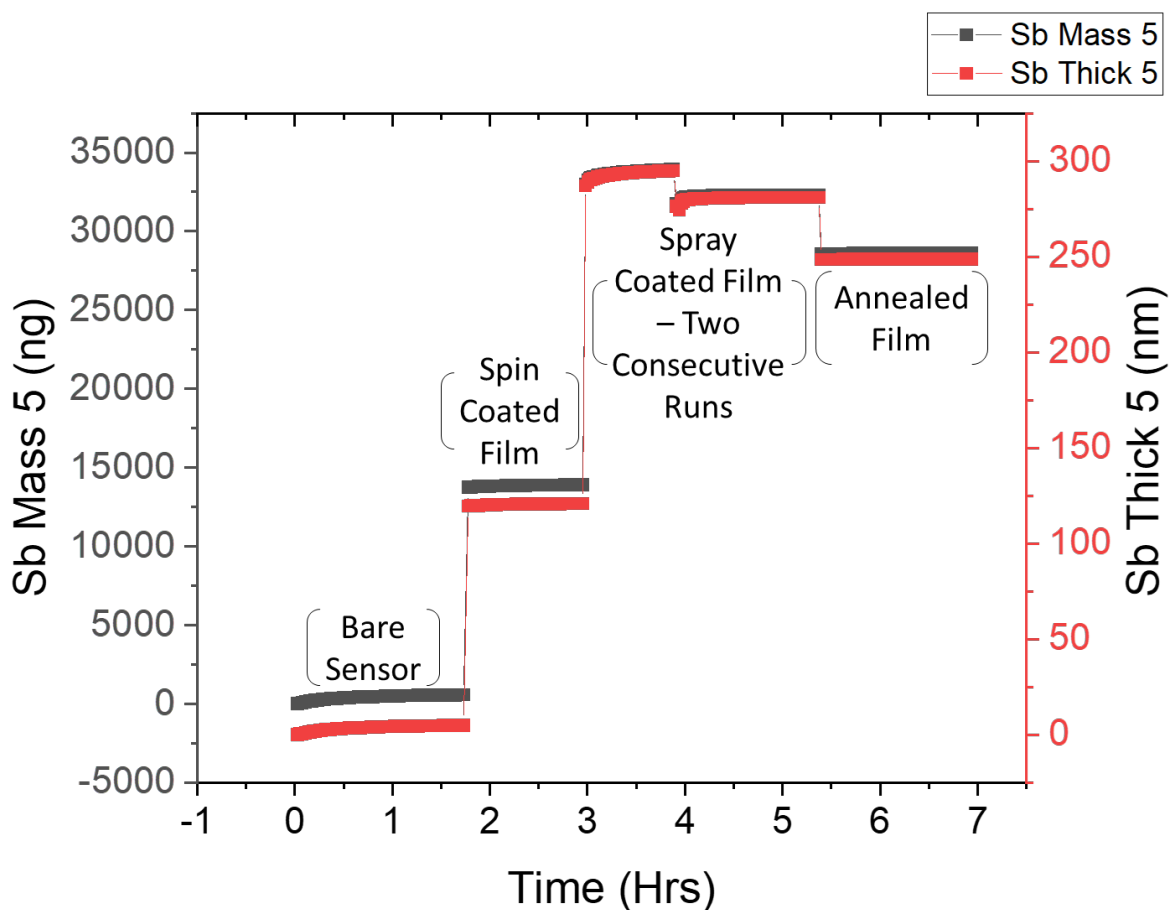
10

Figure 5. Plot of fitted Sauerbrey mass and Sauerbrey thickness vs. time, represented by the gray and red squares, respectively.

Within the spin coated films (S5-S8), the dissipation is small (ΔD ~0). This indicates that the spin coated PS film rigidly adheres to the gold surface upon deposition and displays is indicative of elastic behavior. In this sense, the film is behaving as an extension of the thickness of the quartz sensor. Therefore, the Sauerbrey approximation (**Equation 1**) is used to obtain the thickness, t, of the spin-coated film, and is 120 -140 nm (Δf 740-900 Hz). **Figure 5** shows a plot of the Sauerbrey mass and thickness for S6 as a function of time, corresponding to the five stages in Figure 4. The

effective mass (i.e. areal density) determined via QCM-D for the ESD samples, calculations were compared with mass estimated from the mean particle size (1 and 5 μm for 0.5 and 1.5 mL/h, respectively; from SEM images) and mean shell wall thickness (estimated as 50 and 100 nm, respectively). By assuming a monolayer of PS particles, the theoretical areal density was determined to be 19 and 40 μg/cm^2 for 0.5 and 1.5 mL/h, respectively. These values are in good agreement with mass values obtained from QCM-D measurements (**Table 1)**.

2.2 Viscoelastic and Elastic Modelling

Data from the spray coated films, in which the dissipation was appreciable ($> 1 \times 10^{-7}$ Hz^{-1}), were fit to the Voigt model of viscoelasticity.[23] The Voigt model, in which a spring and a dashpot are arranged in parallel, represents the behavior of an elastic solid undergoing viscoelastic strain. An alternative Maxwell model has a spring and a dashpot arranged in series. When this model is subjected to a stress, the spring deforms immediately while the dashpot deforms linearly with a constant strain-rate. Thus, the model does not predict creep accurately. With prolonged application of a small stress, the strain can become very large, resembling fluid-like behavior.[24] The Voigt model was selected over the Maxwell model by comparing χ^2, a root mean squared goodness of fit, for each data set; the Voigt model reduced χ^2 to 10^{-8}-10^{-10}, compared to 10^{-6}-10^{-8} for the Maxwell model. The choice of the algorithm in minimizing χ^2 has a likely influence on the resulting Voigt mass.[25, 26] Data reported in Table 1 were obtained using QTools software provided by the manufacturer of the instrument.

Table 1. Frequency and dissipation data obtained for all sensors via QCMD.

(No data appear for sensors S1-S4 within Spin Coated section of the table as they were not spin coated)

Sensors	1	2	3	4	5	6	7	8
Rate [mL/hr.]	0.5	0.5	1.5	1.5	0.5	0.5	1.5	1.5
Time [min]	18	18	6	6	18	18	6	6
Spin Coated Films								
Δf [Hz] 5th harmonic	-	-	-	-	-775	-738	-895	-884
ΔD [10^{-6}]	-	-	-	-	0.25	-1.83	-0.23	-0.18
Sauerbrey Mass [µg]	-	-	-	-	14.3	14.3	15.6	16
Voigt Mass [µg]	-	-	-	-	-	-	-	-
t [nm] [r=1050 g/cc]	-	-	-	-	121	121	140	138
Shear Modulus G [MPa]	-	-	-	-	-	-	-	-
Spray Coated Films								
Δf [Hz] 5th harmonic	-1667	-1388	-2717	-2805	-872.4	-1839	-1040	-1187
ΔD [10^{-6}]	43.1	44.4	732	637	2.64	28.6	21.3	133
Sauerbrey Mass [µg]	30	25.5	52.5	52.5	16	34	19	22
Voigt Mass [µg]	23.5	20	52.5	47.5	15.4	30	19.3	26
t [nm] [r= 1050 g/cc]	260	220	416	433	137	295	165	190
Shear Modulus G [MPa]	2.85	2.03	2.34	2.30	80000	5.25	2.15	1.08
Annealed Films								
Δf [Hz] 5th harmonic	-1330	-917.1	-2470	-2746	-833.8	-1633	-1089	-1396
ΔD [10^{-6}]	12.96	-16.4	71.3	105.7	2.59	9.42	8.76	42.35
Sauerbrey Mass [µg]	23.8	19.0	51.0	45.8	15.3	28.3	17.3	26.0
Voigt Mass [µg]	-	-	-	-	-	-	-	-
t [nm][r= 1050 g/cc]	207	166	445	426	132	248	150	225
Shear Modulus G [MPa]	-	-	-	-	-	-	-	-

Shear modulus (G) in the table refers to the complex modulus at megahertz frequencies, consisting of both elastic and inelastic components.[27] G obtained via QCM-D is determined by the phase lag between the input and output signals, and is thus limited to films exhibiting viscoelastic behavior. For a stiff layer rigidly adhered to the sensor surface (no-slip condition at the film-sensor interface), dissipation is negligible.[28] Sauerbrey approximation is used to analyze these data. Therefore, there are no values for Voigt mass or shear moduli in Table 1 for the *Spin Coated Film* and *Thermally Annealed* Films sections. Dramatic decreases in dissipation, similar to that shown here for annealed films, have been observed in QCM-D studies evaluating the collapse of vesicles into lipid bilayers and formation of thin films from nanoparticles upon adsorption.[29, 30] The complex moduli of porous and non-porous polymer films can also be measured by alternative methods such as dynamic mechanical analysis (DMA) and buckling techniques.[31-34] Using these alternative methods, the shear moduli for the spin coated and thermally annealed films can be obtained and compared to that of the spray coated films.[35] Further work is needed to determine whether the moduli obtained from DMA and buckling methods are comparable to the G obtained at MHz frequency through QCM-D measurements. In the data labeled *Spray Coated* in Table I, estimated Voigt mass and dissipation values for sensors S1-S4, in which ESD films were applied directly onto the gold, are similar. However, Sensors S5-S8, which were spin and spray coated, lack this reproducibility in mass and dissipation. There are also inconsistencies in the material properties obtained from sensors, S5-S6 and S7-S8. These results are likely due to variations in the spray process that result in differences of interfacial adhesion between the spin coated and ESD films. The large G (80 GPa) for spray coated sensor S5 is an artifact of the calculations arising from the inadmissible use of Voigt model when the dissipation is small relative to the frequency shift. In contrast, the dissipation in S6-S8 increases by at least an order of magnitude from spin to spray coating, allowing the use of Voigt model.

The characteristics of the ESD samples on gold substrates prepared at similar spray parameters are similar: G values for S1 and S2 are 2.85 and 2.03 MPa, respectively; and S3 and S4 are 2.34 and 2.30 MPa, respectively. The similarities in Voigt mass for the ESD layers on gold surfaces implies that the areal film density, the effective density of the PS shell network, are similar. The characteristics of the ESD samples on spin coated PS substrates prepared at similar spray parameters are different: The difference in *G values* for S7, S8 (2.15 and 1.08 MPa, respectively) could be due to the differences in adhesion between spin and spray coated layers. The significant differences between S5 and S6 (80×10^3 and 5.25 MPa, respectively) is because the Voigt model cannot be used for S5 where dissipation is near zero.[36] Dissipation in the spray coated sensors, S1-S4, appear to be directly proportional to flow rate, with increasing flow rate from 0.5 to 1.5 ml/h leading to increasing dissipation, by five-fold. In contrast, the shear modulus is observed to be independent of flow rate. This could be due to combined effect of change in particle size with flow rate, the changes in the inter-particle contact due to dissimilarity in particle diameters leading to changes in interstitial pore sizes and, perhaps even the limitations of the Voigt model.

2.3 Thermal Annealing

Thermal annealing results in an increase in Δf and a decrease in ΔD in all sensors, indicating that the film layer condenses and behaves more elastically as the PS shells collapse and adhere more rigidly to quartz sensor. This increase in film stiffness is apparent in the *Annealing* section of Table 1. As a result, Voigt model is no longer applicable since the dissipation is negligible as a result of stronger interfacial bonding between the PS film and the quartz crystal sensor. These changes in the QCM-D data upon annealing is corroborated by the work by Keller and Kasemo, who used QCM to study the formation of unilamellar vesicles.[30] The spherical shell-like vesicles illustrated in their work are similar to that of the hollow PS particles shown in Figure 3. While the thinner and more rigidly adhered vesicle monolayers and bilayers observed in Keller and Kasemo's assessment more closely resemble that of the spin coated and annealed

15

films reviewed in this study. Greater dissipation was observed for spherical vesicles, which they ascribed to the structures' ability to undergo larger shear deformation, expressed as a measure of internal friction. Dissipation values for the monolayer and bilayer structures were considered negligible.[30]

Our observations with annealed films are also consistent with the work of Reviakine et al. who reported an increase in Δf and a decrease in ΔD as spherical liposomes collapsed into flat lipid.[37] They used QCM-D can be used to probe the adsorption properties of films consisting of discrete particles with negligible dissipation. Further, they suggested that for layers of laterally heterogenous discrete particles in which dissipation is appreciable, it tends to be dominant at the point of particle-surface contact and the particle-liquid interface.

2.4 Comparison to Bulk Mechanical Properties

Analysis of films produced in the SLED regime typically contain 60-90% porosity, similar to that of extruded polystyrene foams (XPS).[20, 38] Using four-point bending and in-plane shear tests on XPS, Yoshihara and Ataka obtain in-plane shear moduli values between 6.98-9.18 Mpa.[38] While these values are higher than that obtained for the spray coated films in this work (2.03-2.38 MPa), they are surprisingly of similar magnitude. Observable differences may presumably be on account of discrepancies in the underlying polymer and structural properties (*e.g.*, molecular weight and nominal porosity). Strain-rate dependency can also impact these results; while the in-plane shear test might be considered quasi-static, QCM-D is a high-frequency characterization method. Assuming that the sprayed deposited shells are spherical, estimate of the mechanical stiffness of a PS shell can be determined using shell theory.

The shell thickness can be determined using the expression,

$$p = 1 - \left(\frac{V_{shell}}{V_{sphere}} \, v_f \right), \hspace{4cm} 1$$

Where p is porosity, v_f is volume fraction, V_{shell} is the volume of the shell, and V_{sphere} is the spherical volume. For a mean shell diameter of 3.0 μm, v_f=0.65 (consistent with random close

16

packing), and p=0.8, the average shell thickness is 154 nm, which is consistent with SEM measurements of ~100 nm at a flow rate 0.5 mL/hr. For thin curved shells, the elastic strain energy, in terms of the 3D elastic modulus E, can be described by considering the deformation of their middle surface, a 2D manifold. A 2D Young's modulus E_{shell} and, bending rigidity κ, can thus be defined as

$$E_{shell} = Eh \qquad\qquad 2$$

$$\kappa = \frac{Eh^3}{12(1-\nu^2)}, \qquad\qquad 3$$

where h is the thickness of the shell and ν is the Poison's ratio. Note that these properties are strongly scale dependent. The validity of the applying shell theory can be determined by computing the Föppl–von Kármán number, which is given by,

$$\gamma = \frac{E_{shell}D^2}{4\kappa}, \qquad\qquad 4$$

Shell theory is relevant when $h \approx 0.1R$ and $\gamma \geq 1000$.[42-44] Based on the above parameters for spray deposited shells, $h = 85$ nm and $\gamma = 1105$. Bulk PS material is estimated with an average Young's modulus of 3.3 GPa. From Table 1, it is evident that the modulus of spray coated PS is only 0.08-0.20% of the bulk material. The calculated E_{shell} value for a single PS shell is 507 N/m. When comparing the shear modulus (Table 1) with a single shell, the ratio of stiffness of spray coated PS to a single shell is approximately 5.00 - 13.3 x $10^3\,m^{-1}$. The stiffened response of spray coated PS can be attributed to the shell-shell interactions and shell-surface interactions. To quantify the individual contributions of the different interactions, number of shells within spray coated PS, a number of simulation techniques can be used in future work; *e.g.*, Monte Carlo methods, continuum based microscale homogenization methods and coarse-grained molecular dynamics simulations.[39]

Additionally, the effect of areal density can be inferred from the data spray coated sensors. It is suggested that for a given number of sprays coated layers, as the areal density (number of particles per unit area) increases, the dissipation would seemingly increase; as the magnitude of particle-particle interactions would increase, leading to energy losses at particle-particle and particle-substrate interfaces.

With regard to thermal annealing and its influence on the mechanical properties of thin shells, it is important to first consider the scale of stress localization. For curved surfaces, the out-of-plane displacements and in-plane strains are strongly coupled. As a result, the normal deformations tend to be localized to narrow widths in shells. The localized deformation length[40] can by computed by

$$l_e = \frac{D}{2\gamma^{\frac{1}{4}}},$$

5

For spray coated PS shells, $l_e \approx 260nm$. Given the value of stress localization there is greater tendency for the shells to buckle even at room temperatures. Kosmrlj and Nelson showed using perturbative renormalization group theory via a statistical mechanics approach that for curved shells under thermal fluctuations, the 2D elastic parameters scale inversely to the thermal length, l_{th} such that, $\kappa_R \approx \kappa \left(\frac{l}{l_{th}}\right)^{\eta}$ and $E_{shell_R} \approx E_{shell} \left(\frac{l}{l_{th}}\right)^{-\eta_u}$.[41] Where κ_R and E_{shell_R} are the renormalized parameters, the thermal length l_{th} is the length scale where thermal fluctuations become important for flat membranes, l is the length scale of the shells, η and η_u are constants related by the Ward identity, $\eta_u + \eta = 2$.[41] The thermal length can by determined by,

$$l_{th} = \sqrt{\frac{16\pi^3\kappa^2}{3k_B T E_{shell}}},$$

6

where k_B is the Boltzmann's constant and T is the temperature. The critical buckling pressure for spherical shells under the classical theory is given by,

$$p_{cr} = \frac{\sqrt{(\kappa E_{shell})}}{D^2},$$

7

Under thermal fluctuations, the critical buckling pressure can be written in terms of the renormalized parameters,

$$p_{cr_R} = \frac{\sqrt{\left(\kappa_R E_{shell_R}\right)}}{D^2},$$ 8

For the annealed shells heated approximately to the glass transition temperature of 393 K, the ratio of the renormalized critical buckling pressure to the classical pressure is ≈ 0.2. Given the substantial reduction in the magnitude the critical buckling pressure under elevated temperatures, it is safe to postulate that the annealed shells collapse spontaneously due to thermal fluctuations and form a continuous film (Table 1).

Work by Wang and colleagues on modeling viscoelastic contact may indicate that as the number of particles of a given size, all other things held constant, a corresponding of increase in coulombic friction at the particle-particle interfaces would likely increase, leading to more dissipative behavior.[42] However, quantitively decoupling energy dissipation mechanisms in the viscoelastic interactions of discrete particles is beyond the scope of this study and should be explored in future work. This work demonstrates, with further refinement of polymer thin film fabrication and more robust viscoelastic modeling, bulk material properties may be extrapolated from nanogram quantities of polymer materials using QCM-D.

2.5 Limitations of Polymer Film Mechanical Characterization Techniques

Identifying the key deformation mechanisms influencing dissipation in ESD films requires analysis across various spray parameters and loading conditions. Previous studies on the nanoindentation of ESD films (for strain rates $\sim 10^{-1} s^{-1}$) reveal that the collapse of the polymer shell walls and overall particle network are principal failure modes up to $\sim 20\%$ strain, leading to considerable plastic deformation upon unloading.[5] After this threshold, film densification and viscoelastic behavior in the form of creep become significant. Near $\sim 70\%$ strain, the substrate's influence dominates, as indicated by a sharp rise in the load vs. depth curve, showcasing the elastic properties of the rigid Si substrate.[5] Similar behavior was noted by

19

Chung et al. upon the nanoindentation of PS films, in which the plastic zone of deformation extended beyond the thickness of the film, resulting in strong interactions between the film and substrate at the interface, leading to overestimation of the indentation modulus by more than order of magnitude.[43] Herbert et al assess experimental methods for probing the viscoelastic behavior of polymers subject to oscillating loads between 0-300 Hz.[44] However, there is a dearth of literature comparing moduli values obtained at low frequencies (10^0-10^3 Hz) to the MHz frequencies encountered in QCM-D. Future work should compare moduli obtained from dynamic nanoindentation of viscoelastic particles subject to harmonic loading to the complex moduli resulting from QCM-D for polymer particles.

In addition, LIPIT has been used to assess the mechanical performance of ESD films subject to high strain rates (10^1-10^6 s^{-1}).[17] The observed dissipation under these conditions was attributed to the collapse of the porous film and thermo-mechanical melting. For some samples under high-speed conditions (>700 m/s), substrate interactions had significant influence on the material and structural behavior of the films, and infrequently led to complete disintegration of the impacting particle.[17] Both LIPIT and nanoindentation exhibit experimental limitations due to nanoparticle confinement at the substrate interface, resulting from the geometric constraints of the impacting particle and indenter tip, respectively. QCM-D facilitates characterization of the complex moduli and dissipative response of polymeric materials yet is not subject to the geometric limitations observed in LIPIT and nanoindentation due to its loading configuration. Thus, QCM-D provides an auxiliary method of mechanical characterization at high strain rates. To this end, ESD was performed under ambient conditions to demonstrate its potential for easy manufacturing of tunable micro/nanoparticles layers. However, variations in ESD processing, especially when applied to the spin coat PS films, can lead to a lack of uniformity at the coating interface. Future work could mitigate this by controlling environmental conditions during ESD, such as substrate-temperature, humidity, and the electrostatic "charge landscape," similar to what has been conducted in recent demonstrations in ESD for bioactive coatings[45] and sub-

20

micron deposition. Further research is necessary to accurately model the mechanical behavior of such films, particularly for applications involving protein adsorption onto ESD films.[46]

3. Conclusion

In this work, QCM-D was used to analyze viscoelastic behavior of polymer shells of varying sizes produced by ESD and subject to MHz range shear oscillations. ESD films deposited directly onto bare quartz sensors exhibit larger shifts in dissipation compared to sprayed films deposited onto smooth PS films for all flow rates. Films electrosprayed at 1.5 mL/h showed two times the Δf and an order of magnitude increases in ΔD compared to the films deposited at 0.5 mL/h. The larger shifts in Δf and ΔD are caused by increased particle diameters produced at higher flow rates, attributed to a higher degree of shear deformation and internal friction. Films produced a 0.5 mL/h behaved more elastically, owing to a shorter in interparticle distance and an increase in interparticle fusion due to localized region of unevaporated solvent. Data obtained from Voigt model analysis reveal that, the shear moduli of ESD films are flow rate independent within experimental error. The Sauerbrey model was used to estimate the properties of the spin coat and thermally annealed PS coatings. However, neither the Sauerbrey nor Voigt model obtained reproducible results for ESD films deposited onto smooth PS films. Further work is needed to develop more robust mechanical models for complex multilayer films that can account for the behavior of multilayers discrete particles exhibiting viscoelastic behavior. A comparison of the observed mechanical characteristics on shells at high frequencies to the static bulk properties show that the observed modulus is 0.002 times the bulk modulus but is 5-10 thousand times stiffer than a single shell because interfacial interactions between the shells and the substrate.

Unlike LIPIT and nanoindentation, QCM-D offers the ability to evaluate the viscoelastic properties of ESD films without the limitations of size dependent artifacts arising from the impacting particle or indenter tip, respectively. Additionally, confinement effects often seen in mechanical characterization of nanoparticles on rigid substrates, appears to be negligible for

21

QCM-D; resulting from shear induced deformation as opposed to a loading condition normal to the surface of the film, as is the case in atomic force microscopy (AFM), LIPIT, and nanoindenation.[47, 48]

Future work can look to develop models of coupled storage and loss elements comparable to dynamic mechanical analysis (DMA). Applications of ESD and QCM-D in tandem could serve as a novel method for facile fabrication and evaluation of polymer separators, solid polyelectrolytes, or hybrid polymer electrodes for use in solid state batteries. Further, a parametric study is recommended to optimize film deposition techniques so QCM-D can be used to develop ESD sensors with tunable size selectivity for nanogram quantities of gases, liquids, or bioactive particles.

4. Experimental Section

Sample Fabrication:
The results from one of the five experiments are being reported here. The five experiments were carried out with small changes in the electrospraying protocol to improve the quality of the deposition. The results from all the experiments were similar, demonstrating the reproducibility of the fabrication and measurement procedures. ESD was used to deposit polystyrene (PS) [molecular weight (MW) = 35 kDa] (Millipore Sigma, USA) shells onto gold plated quartz crystal sensors as described in previous work.[5] A 1 wt.% solution of PS in 2-butanone (MEK) (Millipore Sigma, USA) was chosen due to produce tunable nano/microscale particles. ESD parameters were selected to ensure stability of the Taylor cone, and to produce microscale PS particles of varying sizes.[5, 49] During the spray process, each quartz crystal was adhered to a 100 cm p-type boron doped silicon wafer [0-100 Ω-cm] (University Wafer, USA) using a drop of deionized water to improve the interfacial contact between the bottom of the sensor and the top of the wafer. The wafer was then mounted on an aluminum plate and electrically grounded. The substrates were sprayed at ambient conditions (~20ºC) and 20-50%

22

relative humidity. The ability to spray this solution in ambient humidity is ostensibly enabled by the hydrophobic nature of the phenyl and methyl functional groups of the PS and MEK, respectively.[50, 51] The nozzle and extractor ring distances and voltages were 4 and 5 cm, and 6 and 4 kV, respectively.

SEM Characterization:

Si wafer chips (1 cm x 1 cm) were sprayed with PS at the given spray parameters in ambient conditions. Gold sputtering was used to deposit 10 nm of Au onto the PS particles. SEM images were taken with a 5kV driving voltage in a Zeiss Sigma FESEM with EBSD (Zeiss, Germany), and the microstructure is observed.

QCMD Experimental Procedures:

QCM-D measurements were carried out on a QSense Pro instrument (Biolin Scientific, Sweden). Bare Au-plated quartz crystals were first measured to establish a baseline frequency and dissipation prior to sequential spin coating, electrospraying, and finally, thermal annealing. Sensors 1-8 (S1-S8) were prepared as follows: S5-S8 were spin coated with a 5% MEK solution of PS at 2000 RPM for 30 s to presumably provide improved interfacial contact with the ESD films, initially thought to be enhanced by solvent vapor swelling. S1, S2, S5, and S6 were sprayed at 0.5 mL/h for 18 minutes, while S3, S4, S7, and S8 were all sprayed at 1.5 mL/h for 6 minutes. All samples were sprayed with 0.15 mL of 1 wt.% PS solution to ensure uniform mass deposition, but at different flow rates to achieve PS particles of varying sizes.

Thermal Annealing:

After obtaining QCM-D data from the spray-coated samples, all samples were thermally annealed on a hotplate at 120ºC (above the T_g of PS) for ~10 minutes to smooth the particles into a continuous film. Frequency and dissipation data were obtained on these smoothed thin films.

QCMD Data Analysis:

23

Frequency and dissipation data from all the steps were stitched together and analyzed using QTools analysis software. QCM-D data are typically presented as the changes in the frequency of oscillation of the quartz sensor crystal (Δf), and the changes in ΔD.[18, 19, 52] If ΔD (which reflects the time-dependent properties of the deposited layers) is small, then Δf can be used determine the adsorbed mass (Δm). A decrease in frequency indicates adsorption of mass, and conversely an increase indicates mass loss, as given by the Sauerbrey equation:

$$\Delta m = -\left(\frac{C}{n}\right)\Delta f \qquad (1)$$

where C is the mass sensitivity constant (17.7 ng/cm^2), and n is the overtone number (1, 3, …,13).[52] ΔD was small in many instances, but in some instances, it was between 0.8 and 1.6 x 10^{-6} units. This is higher than the commonly accepted threshold proposed by Reviakine et al., $\left|\frac{\Delta D}{\Delta f_n}\right| < 4$ x 10^{-7} Hz^{-1}, for applying the Sauerbrey equation.[37, 53] When ΔD was large, $\left|\frac{\Delta D}{\Delta f_n}\right| > 4$ x 10^{-7} Hz^{-1}, the Voigt viscoelastic model was used to analyze the data and obtain the adsorbed thickness (assuming an effective density of 1050 kg$^{\circ}$cm^{-3}) and shear modulus of the electrosprayed layer.[52]

Supporting Information

A PDF of the raw and fitted QCMD data plots are available in the Wiley Online Library or from the author.

Conflict of Interest Statement

J.P.S. is coinventor of three patents/applications on self-limiting electrospray deposition. Otherwise, the Authors have no conflict of interest relevant to this article.

N. Sanjeeva Murthy

ORCID: 0000-0002-2324-5874

Jonathan. P. Singer

ORCID: 0000-0002-5934-8795

Robert A. Green-Warren

ORCID: 0000-0002-3842-2140

Assimina A. Pelegri

ORCID: 0000-0003-1145-8175

25

References

1. A. K. Hołda and I. F. J. Vankelecom, *Journal of Applied Polymer Science*, 2015, **132**.
2. D. T. W. Toolan, E. u. Haq, A. Dunbar, S. Ebbens, N. Clarke, P. D. Topham and J. R. Howse, *Journal of Polymer Science Part B: Polymer Physics*, 2013, **51**, 875-881.
3. G. I. Taylor, *Proceedings of the Royal Society of London. Series A. Mathematical and Physical Sciences*, 1964, **280**, 383-397.
4. L. Lei, D. A. Kovacevich, M. P. Nitzsche, J. Ryu, K. Al-Marzoki, G. Rodriguez, L. C. Klein, A. Jitianu and J. P. Singer, *ACS Applied Materials & Interfaces*, 2018, **10**, 11175-11188.
5. R. A. Green-Warren, L. Bontoux, N. M. McAllister, D. A. Kovacevich, A. Shaikh, C. Kuznetsova, M. Tenorio, L. Lei, A. A. Pelegri and J. P. Singer, *ACS Applied Polymer Materials*, 2022, **4**, 3511-3519.
6. D. A. Kovacevich, L. Lei, D. Han, C. Kuznetsova, S. E. Kooi, H. Lee and J. P. Singer, *ACS Applied Materials & Interfaces*, 2020, **12**, 20901-20911.
7. B. J. Kingsley and P. R. Chiarot, *ACS Applied Polymer Materials*, 2023, **5**, 1797-1809.
8. J. Tang and A. Gomez, *Aerosol Science and Technology*, 2017, **51**, 755-765.
9. J. Y. Kim and J. G. Hong, *Journal of Applied Fluid Mechanics*, 2022, **15**, 1427-1436.
10. L. Lei, S. Chen, C. J. Nachtigal, T. F. Moy, X. Yong and J. P. Singer, *Materials Horizons*, 2020, **7**, 2643-2650.
11. I. R. Jang, S. I. Jung, J. Park, C. Ryu, I. Park, S. B. Kim and H. J. Kim, *Ceramics International*, 2022, **48**, 8004-8011.
12. L. Lei, A. R. Gamboa, C. Kuznetsova, S. Littlecreek, J. Wang, Q. Zou, J. D. Zahn and J. P. Singer, *Scientific Reports*, 2020, **10**, 17290.
13. N. A. Brown, Y. Zhu, G. K. German, X. Yong and P. R. Chiarot, *Journal of Electrostatics*, 2017, **90**, 67-73.
14. J. M. Blisko, M. J. Grzenda, R. M. Vladimirsky, C. E. Shuck, J. P. Singer and X. Yong, *Nanoscale*, 2022, **14**, 17985-17994.
15. S. Morais AÍ, E. G. Vieira, S. Afewerki, R. B. Sousa, L. M. C. Honorio, A. Cambrussi, J. A. Santos, R. D. S. Bezerra, J. A. O. Furtini, E. C. Silva-Filho, T. J. Webster and A. O. Lobo, *J Funct Biomater*, 2020, **11**.
16. J.-H. Lee, D. Veysset, J. P. Singer, M. Retsch, G. Saini, T. Pezeril, K. A. Nelson and E. L. Thomas, *Nature Communications*, 2012, **3**, 1164.
17. Z. Ren, R. Green-Warren, N. McAllister, A. Kim, A. Shaikh, A. A. Pelegri, J. P. Singer and J.-H. Lee, *Giant*, 2023, **15**, 100180.
18. M. C. Dixon, *J Biomol Tech*, 2008, **19**, 151-158.
19. A. Tarnapolsky and V. Freger, *Analytical Chemistry*, 2018, **90**, 13960-13968.
20. N. McAllister, R. Green-Warren, M. Arkhipov, J.-H. Lee, A. Pelegri and J. Singer, *Non-Destructive Measurement of Optically Scattering Polymer Films Using Image Processing*, 2023.
21. R. M. Green-Warren, Noah;Arkhipov, Maxim;Singer, Jonathan, Electrostatic Generation of Sprays and Filaments, Bulletin of the American Physical Society, 2023.
22. A. M. Gañán-Calvo, J. Dávila and A. Barrero, *Journal of Aerosol Science*, 1997, **28**, 249-275.
23. A. D. Easley, T. Ma, C. I. Eneh, J. Yun, R. M. Thakur and J. L. Lutkenhaus, *Journal of Polymer Science*, 2022, **60**, 1090-1107.
24. T. E. Alexander, L. D. Lozeau and T. A. Camesano, *The Cell Surface*, 2019, **5**, 100024.

25. A. Saftics, G. A. Prósz, B. Türk, B. Peter, S. Kurunczi and R. Horvath, *Scientific Reports*, 2018, **8**, 11840.
26. I. Furikado, J. Forsman and T. Nylander, *Analytical Chemistry*, 2023, **95**, 15286-15292.
27. E. F. Irwin, J. E. Ho, S. R. Kane and K. E. Healy, *Langmuir*, 2005, **21**, 5529-5536.
28. D. Johannsmann, A. Langhoff and C. Leppin, *Sensors*, 2021, **21**, 3490.
29. A. Patel, M. R. N. Lima, H.-Y. Cho, K.-B. Lee, N. S. Murthy and J. Kohn, *Langmuir*, 2020, **36**, 232-241.
30. C. A. Keller and B. Kasemo, *Biophysical Journal*, 1998, **75**, 1397-1402.
31. C. K. Huang, W. M. Lou, C. J. Tsai, T.-C. Wu and H.-Y. Lin, *Thin Solid Films*, 2007, **515**, 7222-7226.
32. C. M. Stafford, C. Harrison, K. L. Beers, A. Karim, E. J. Amis, M. R. VanLandingham, H.-C. Kim, W. Volksen, R. D. Miller and E. E. Simonyi, *Nature Materials*, 2004, **3**, 545-550.
33. K.-i. Akabori, K. Tanaka, T. Nagamura, A. Takahara and T. Kajiyama, *Macromolecules*, 2005, **38**, 9735-9741.
34. S. H. K. Paleti, Y. Kim, J. Kimpel, M. Craighero, S. Haraguchi and C. Müller, *Chemical Society Reviews*, 2024, **53**, 1702-1729.
35. W.-E. Fu, Y.-Q. Chang, B.-C. He and C.-L. Wu, *Thin Solid Films*, 2013, **544**, 201-205.
36. J. Petri and D. Johannsmann, *Analytical Chemistry*, 2019, **91**, 1595-1602.
37. I. Reviakine, D. Johannsmann and R. P. Richter, *Analytical Chemistry*, 2011, **83**, 8838-8848.
38. H. Yoshihara, N. Ataka and M. Maruta, *Journal of Cellular Plastics*, 2018, **54**, 199-216.
39. Q. H. Zeng, A. B. Yu and G. Q. Lu, *Progress in Polymer Science*, 2008, **33**, 191-269.
40. J. Paulose and D. R. Nelson, *Soft Matter*, 2013, **9**, 8227-8245.
41. A. Košmrlj and D. R. Nelson, *Physical Review X*, 2017, **7**, 011002.
42. D. Wang, G. de Boer, A. Neville and A. Ghanbarzadeh, *Lubricants*, 2022, **10**, 358.
43. P. C. Chung, E. Glynos and P. F. Green, *Langmuir*, 2014, **30**, 15200-15205.
44. E. G. Herbert, P. Sudharshan Phani and K. E. Johanns, *Current Opinion in Solid State and Materials Science*, 2015, **19**, 334-339.
45. S. H. Park, L. Lei, D. D'Souza, R. Zipkin, E. T. DiMartini, M. Atzampou, E. O. Lallow, J. W. Shan, J. D. Zahn, D. I. Shreiber, H. Lin, J. N. Maslow and J. P. Singer, *Nature Communications*, 2023, **14**, 4896.
46. A. Rouf, S. H. Park and J. P. Singer, *Advanced Materials Interfaces*, **n/a**, 2300982.
47. H. Wang, Y. Qiang, A. A. Shamsabadi, P. Mazumder, K. T. Turner, D. Lee and Z. Fakhraai, *ACS Macro Letters*, 2019, **8**, 1413-1418.
48. J. Song, R. Kahraman, D. W. Collinson, W. Xia, L. C. Brinson and S. Keten, *Soft Matter*, 2019, **15**, 359-370.
49. I. N. Sneddon, *International Journal of Engineering Science*, 1965, **3**, 47-57.
50. J. J. Barchi, Jr. and C. N. Strain, *Front Mol Biosci*, 2023, **10**, 1117850.
51. J. M. Kim, Y.-H. Lin, P. P. Aravindhan and B. S. Beckingham, *Chemical Engineering Research and Design*, 2022, **185**, 418-429.
52. F. Höök, B. Kasemo, T. Nylander, C. Fant, K. Sott and H. Elwing, *Analytical Chemistry*, 2001, **73**, 5796-5804.
53. K. Sadman, C. G. Wiener, R. A. Weiss, C. C. White, K. R. Shull and B. D. Vogt, *Analytical Chemistry*, 2018, **90**, 4079-4088.

27

28